Modeling and Stability Analysis of Radial and Zonal Architectures of a Bipolar DC Ferry Ship

Yadav, Sachin; van der Blij, Nils H.; Bauer, Pavol

DOI
10.1109/ESTS49166.2021.9512334

Publication date
2021

Document Version
Accepted author manuscript

Published in
2021 IEEE Electric Ship Technologies Symposium, ESTS 2021

Citation (APA)
Yadav, S., van der Blij, N. H., & Bauer, P. (2021). Modeling and Stability Analysis of Radial and Zonal Architectures of a Bipolar DC Ferry Ship. In *2021 IEEE Electric Ship Technologies Symposium, ESTS 2021: Proceedings* Article 9512334 IEEE. https://doi.org/10.1109/ESTS49166.2021.9512334

Modeling and Stability Analysis of Radial and Zonal Architectures of a Bipolar DC Ferry Ship

Sachin Yadav
DC Energy Conversion and Storage
TU Delft
Delft, The Netherlands
S.Yadav-1@tudelft.nl

Nils H van der Blij
DC Energy Conversion and Storage
TU Delft
Delft, The Netherlands
N.H.vanderBlij@tudelft.nl

Pavol Bauer
DC Energy Conversion and Storage
TU Delft
Delft, The Netherlands
P.Bauer@tudelft.nl

2021 IEEE Electric Ship Technologies Symposium (ESTS) | 978-1-7281-8426-5/21/$31.00 ©2021 IEEE | DOI: 10.1109/ESTS49166.2021.9512334

***Abstract*—Electrification of ships is one of the hot topics in the marine industry. This is due to the stringent guidelines by the International Maritime Organisation (IMO) for curbing the green house gas emissions from the marine sector. In this paper, the state-space modeling approach is used to model bipolar dc grids on ships. A ferry is used as a test case. The modeling is done for the radial and zonal architecture with similar components. The dynamic simulation and stability analysis of the two architectures reveal that zonal architecture is potentially more stable than the radial architecture.**

***Index Terms*—bipolar, dc, grids, ships, modeling, state-space, radial, zonal**

I. Introduction

Climate change is one of the major concerns of human civilisation right now. In the purview of the marine sector, the International Maritime Organisation (IMO) has setup strict guidelines to curb the green house gas emissions from marine vessels [1]. Hence, the whole sector is engaged in improving the efficiency of operation aboard a marine vessel. Apart from climate change, there are also issues relating to the increased fuel prices that makes the operation more expensive. The push from the global organisation for sustainable shipping is also a major reason for moving towards a more green marine sector [2].

Electrification of marine vessels is one of the major ways to improve the efficiency of operation [3] [4]. The future electric ship architecture is expected to be based on dc. This is because of the following advantages: [5] [6] [7]

- Lower losses due to the absence of reactive power and skin effect in dc.
- Reduction of size of passive components because of high frequency power conversion.
- Ease of integration of renewable energy resources since batteries and PV produce dc power.

Compared to a unipolar dc grid, a bipolar dc grid has many advantages. These are as follows [8] [9]

- A bipolar dc grid has a higher power transmission capacity per mm^2 compared to a unipolar grid. This is because in a bipolar grid, three conductors are required instead of four to transfer the same amount of power at the same voltage.
- A unipolar grid can provide a single voltage level in the system. On the other hand, a bipolar grid can provide more than one voltage levels by connecting device at different terminals namely positive and negative $(+-)$ poles, positive and neutral $(+n)$ poles, and neutral and negative $(n-)$ poles.
- The robustness of a bipolar dc grid is higher than that of a unipolar grid. This is because a bipolar can still function with half power capacity when there is a fault on one of the poles.

The implementation of bipolar dc grids on ships is quite limited. This is because of the lack of information and commercially off the shelf components. Therefore, there is a pressing need to understand the behaviour of these grids. In this paper, a state-space modeling approach has been used to model bipolar dc grids aboard a ferry vessel. Two different architectures – radial and zonal – are simulated using this method. Also, the stability analysis is done to compare the two architectures.

The structure of the paper is as follows. In section II, the model of various components of a bipolar dc grid are discussed. The system equations of a general dc grid system are also discussed. In section III, the state-space modeling approach is discussed. In section IV, the stability analysis of dc grid is briefly discussed. In section V, the radial and zonal architecture developed for a ferry are discussed. In section VI, the test case for comparing the two architectures is discussed. In section VII, the results are discussed. The paper is concluded in section VIII.

II. Modeling of bipolar dc grids

The modeling of a system helps in understanding the behavior of the system under normal and abnormal operating conditions. There are several methods of modeling a system. The utility of these methods depends upon the amount of insight that is required [10].

A. Line modeling

In the dynamic modeling method, the distribution lines are modelled as π-sections as shown in Fig. 1. This model also includes the mutual line elements such as the mutual inductance between the lines and the line-to-line capacitance.

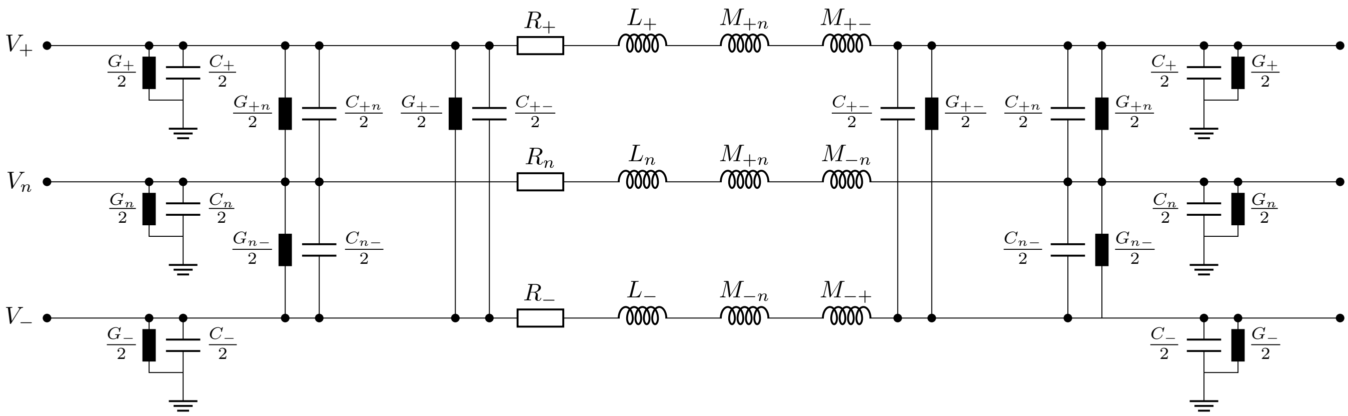

Fig. 1: Lumped element π-model of a bipolar distribution line [10].

The π-model can be used for short line lengths since the propagation delays can be neglected [11].

B. Converter modeling

The converters are modelled as ideal converters. The grid forming converter has a droop controller for controlling the current output/input. The current injected by the droop controlled converter and load converters are shown by

$$I_d = \frac{U_o - U_i}{Z_d}, \tag{1}$$

$$I_l = -\frac{P_l}{U_i}, \tag{2}$$

where U_o is the reference voltage, U_i is the voltage at the converter connection node, Z_d is the virtual droop impedance, and P_l is the power consumed by the load.

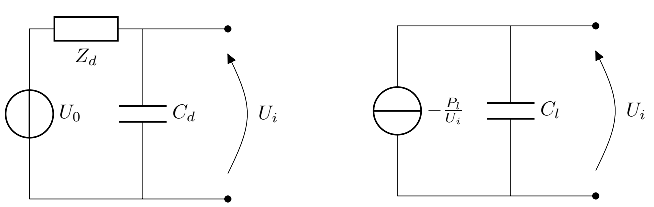

(a) Droop controlled converter (b) CPL converter

Fig. 2: Idealized model for droop controlled and constant power load converters.

The ideal and linearized models for the droop controlled sources are shown in Fig. 2a and 4a respectively. The ideal and linearized models for the constant power load converters are shown in Fig. 2b and 4b respectively.

C. Grid modeling

A grid can be represented by a combination of lines and nodes. The lines consist of cables between nodes. There can be more than one conductor in a line. The π-model of a line with three conductors is shown in Fig. 1. An incidence matrix is used to represent the connection between the lines and nodes.

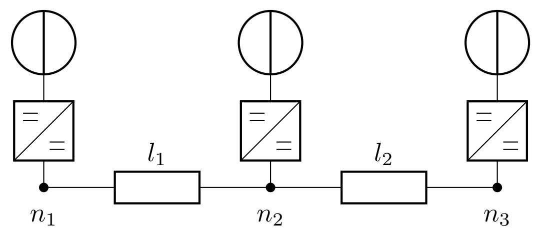

Fig. 3: Model representing a 3 node 2 line 1 conductor system.

For a small system of nodes and lines shown in Fig. 3, the incidence matrix is given by (3). The columns of the incidence matrix represent the nodes in the system; the rows of the incidence matrix represent the lines in the system. The current from a node into a line is represented as 1; the current into a node from a line is represented as -1. It is important to state here that this convention is chosen arbitrarily and the signs can be opposite.

$$\gamma = \begin{bmatrix} 1 & -1 & 0 \\ 0 & 1 & -1 \end{bmatrix} \tag{3}$$

If there are three conductor instead of one in the same system, the size of the incidence matrix changes. In that case, the incidence matrix will contain 3x3 columns representing the nodes and 3x2 rows representing the lines. The incidence matrix $\mathbf{\Gamma}$ for a three node, two lines, three conductor system is given in (4).

$$\mathbf{\Gamma} = \begin{bmatrix} 1 & 0 & 0 & -1 & 0 & 0 & 0 & 0 & 0 \\ 0 & 1 & 0 & 0 & -1 & 0 & 0 & 0 & 0 \\ 0 & 0 & 1 & 0 & 0 & -1 & 0 & 0 & 0 \\ 0 & 0 & 0 & 1 & 0 & 0 & -1 & 0 & 0 \\ 0 & 0 & 0 & 0 & 1 & 0 & 0 & -1 & 0 \\ 0 & 0 & 0 & 0 & 0 & 1 & 0 & 0 & -1 \end{bmatrix} \tag{4}$$

D. System equations

For a dc distribution system, the KCL and KVL equations are used to create the equations for state-space representation. The chosen state variables are the node voltages and the line currents. The KCL equation is used to derive the state equation for the node voltages. The voltage across the capacitances connected to a node is related to the net current flowing through that node. Hence, applying the KCL at a node $\boldsymbol{N}$, we get

$$\boldsymbol{C}\dot{\boldsymbol{U}}_{\boldsymbol{N}} = \boldsymbol{I}_{net}. \tag{5}$$

Expanding (5) to include the line currents $\boldsymbol{I_L}$, node currents $\boldsymbol{I_N}$ (injected/extracted by the power converters/loads), and conductance currents, we get

$$\boldsymbol{C}\dot{\boldsymbol{U}}_{\boldsymbol{N}} = \boldsymbol{I_N} - \boldsymbol{\Gamma^T I_L} - \boldsymbol{G U_N}. \tag{6}$$

The KVL equations are used to derive the state equations for the line currents. The current flowing through the line inductance is dependent upon the difference between the node voltages. Hence, applying KVL between two nodes connected by a line, we get

$$\boldsymbol{L}\dot{\boldsymbol{I}}_{\boldsymbol{L}} = \boldsymbol{U_L}. \tag{7}$$

Expanding (7) to include the voltage drop across the line resistances, we get

$$\boldsymbol{L}\dot{\boldsymbol{I}}_{\boldsymbol{L}} = \boldsymbol{\Gamma U_L} - \boldsymbol{R I_L}. \tag{8}$$

III. State-space model

A. Model representation

State-space modeling can be used to model linear time-invariant systems in the form of first order differential equations [12]. The basic form of state-space model is given by

$$\dot{\boldsymbol{x}} = \boldsymbol{A x} + \boldsymbol{B u}. \tag{9}$$

The observation equation is given by

$$\boldsymbol{y} = \boldsymbol{D x} + \boldsymbol{E u}, \tag{10}$$

where $\boldsymbol{x}$ is the state vector, $\boldsymbol{u}$ is the input to the system, $\boldsymbol{y}$ is the system output vector, and $\boldsymbol{ABDE}$ are the state-space matrices.

In the purview of our system, the state vector consists of the node voltages and line currents which is given by

$$\boldsymbol{x} = [U_{1,1} \quad U_{1,2} \quad \dots \quad U_{n,m} \quad I_{1,1} \quad I_{1,2} \quad \dots \quad I_{l,m}], \tag{11}$$

where n is the number of nodes, l is the number of lines, and m is the number of conductors per line. Similarly, the input vector $\boldsymbol{u}$ of the system consists of the node currents injected/extracted by the power converters is given by

$$\boldsymbol{u} = [I_{N,1,1} \quad I_{N,1,2} \quad \dots \quad I_{N,n,m}]. \tag{12}$$

Equations (6) and (8) can be rearranged to form the first order differential equations given by

$$\dot{\boldsymbol{U}}_{\boldsymbol{N}} = \boldsymbol{C^{-1} I_N} - \boldsymbol{C^{-1}\Gamma^T I_L} - \boldsymbol{C^{-1} G U_N}, \tag{13}$$

$$\dot{\boldsymbol{I}}_{\boldsymbol{L}} = \boldsymbol{L^{-1}\Gamma U_L} - \boldsymbol{L^{-1} R I_L}. \tag{14}$$

Accordingly, the state-space matrices can be defined as

$$\boldsymbol{A} = \begin{bmatrix} -\boldsymbol{C^{-1}G} & -\boldsymbol{C^{-1}\Gamma^T} \\ \boldsymbol{L^{-1}\Gamma} & -\boldsymbol{L^{-1}R} \end{bmatrix}, \tag{15}$$

$$\boldsymbol{B} = \begin{bmatrix} -\boldsymbol{C^{-1}} \\ \emptyset \end{bmatrix}, \tag{16}$$

$$\boldsymbol{D} = \boldsymbol{I}, \tag{17}$$

$$\boldsymbol{E} = \emptyset. \tag{18}$$

B. Definition of state-space matrices

The details about the creation of the $\boldsymbol{R, L, C, G}$ matrices are given in this section. There is a two-step procedure for creating the matrices. In the first step, the matrices are calculated for each line l with m conductors.

$$\boldsymbol{R_{L,l}} = \begin{bmatrix} R_1 & 0 & \dots & 0 \\ 0 & R_2 & \ddots & 0 \\ \vdots & \ddots & \ddots & 0 \\ 0 & \dots & 0 & R_m \end{bmatrix},$$

$$\boldsymbol{L_{L,l}} = \begin{bmatrix} L_{11} & M_{12} & \dots & M_{1m} \\ M_{21} & L_{22} & \ddots & M_{2m} \\ \vdots & \ddots & \ddots & M_{(m-1)m} \\ M_{m1} & \dots & M_{m(m-1)} & L_{mm} \end{bmatrix}, \tag{19}$$

$$\boldsymbol{C_{L,l}} = \begin{bmatrix} \sum_{k=1}^{m} C_{1k} & -C_{12} & \dots & -C_{1m} \\ -C_{21} & \sum_{k=1}^{m} C_{2k} & \ddots & -C_{2m} \\ \vdots & \ddots & \ddots & -C_{(m-1)m} \\ -C_{m1} & \dots & -C_{m(m-1)} & \sum_{k=1}^{m} C_{mk} \end{bmatrix},$$

$$\boldsymbol{G_{L,l}} = \begin{bmatrix} \sum_{k=1}^{m} G_{1k} & -G_{12} & \dots & -G_{1m} \\ -G_{21} & \sum_{k=1}^{m} G_{2k} & \ddots & -G_{2m} \\ \vdots & \ddots & \ddots & -G_{(m-1)m} \\ -G_{m1} & \dots & -G_{m(m-1)} & \sum_{k=1}^{m} G_{mk} \end{bmatrix}. \tag{20}$$

The nodal matrices from the line matrices can be calculated using the incidence matrix $\boldsymbol{\Gamma}$. This is because $\boldsymbol{\Gamma}$ also gives the relationship of the connection of all lines with all the nodes. The nodal matrix can be calculated as

$$\boldsymbol{C_{N,n}} = \frac{1}{2}|\boldsymbol{\Gamma^T}| \sum_{j=1}^{l} \boldsymbol{C_{L,j}}, \tag{21}$$

$$G_{N,n} = \frac{1}{2}|\Gamma^T| \sum_{j=1}^{l} G_{L,j}. \tag{22}$$

In the next step, each of the matrices with respect to the lines are combined to form the final matrices as

$$\boldsymbol{R} = \begin{bmatrix} \boldsymbol{R_{L,1}} & 0 & \dots & 0 \\ 0 & \boldsymbol{R_{L,2}} & \ddots & 0 \\ \vdots & \ddots & \ddots & 0 \\ 0 & \dots & 0 & \boldsymbol{R_{L,l}} \end{bmatrix},$$

$$\boldsymbol{L} = \begin{bmatrix} \boldsymbol{L_{L,1}} & 0 & \dots & 0 \\ 0 & \boldsymbol{L_{L,2}} & \ddots & 0 \\ \vdots & \ddots & \ddots & 0 \\ 0 & \dots & 0 & \boldsymbol{L_{L,l}} \end{bmatrix},$$

$$\boldsymbol{C} = \begin{bmatrix} \boldsymbol{C_{N,1}} & 0 & \dots & 0 \\ 0 & \boldsymbol{C_{N,2}} & \ddots & 0 \\ \vdots & \ddots & \ddots & 0 \\ 0 & \dots & 0 & \boldsymbol{C_{N,n}} \end{bmatrix},$$

$$\boldsymbol{G} = \begin{bmatrix} \boldsymbol{G_{N,1}} & 0 & \dots & 0 \\ 0 & \boldsymbol{G_{N,2}} & \ddots & 0 \\ \vdots & \ddots & \ddots & 0 \\ 0 & \dots & 0 & \boldsymbol{G_{N,n}} \end{bmatrix}. \tag{23}$$

IV. Stability Analysis

In a dc grid, the loads are interfaced with power converter that are tightly regulated to work as constant power loads. Constant power loads show a negative impedance behavior which has the tendency of making a system unstable [13]. Hence, it is necessary to evaluate stability of the whole system with respect to the impedance of the converters. The small signal linearized Norton equivalent of the droop controlled source converters and constant power load converters are shown in Fig. 4a and 4b respectively. The generalized form of current injected/ejected from these converters is given by

$$I_i = I_{i,0} - \frac{1}{Z_i} U_i, \tag{24}$$

where $I_{i,0}$ is the linearized current to/from converter, Z_i is the linearized converter impedance and U_i is the voltage converter input terminals.

Combining (24) with (13), we can write the state-space equation as [14]

$$\begin{bmatrix} \dot{\boldsymbol{U}}_{\boldsymbol{N}} \\ \dot{\boldsymbol{I}}_{\boldsymbol{L}} \end{bmatrix} = \begin{bmatrix} -\boldsymbol{C}^{-1}\boldsymbol{Z}^{-1} & -\boldsymbol{C}^{-1}\boldsymbol{\Gamma}^{\boldsymbol{T}} \\ \boldsymbol{L}^{-1}\boldsymbol{\Gamma} & -\boldsymbol{L}^{-1}\boldsymbol{R} \end{bmatrix} \begin{bmatrix} \boldsymbol{U_N} \\ \boldsymbol{I_L} \end{bmatrix} + \begin{bmatrix} \boldsymbol{C}^{-1} \\ \emptyset \end{bmatrix} \boldsymbol{I_{N,0}}. \tag{25}$$

The state-matrix $\boldsymbol{A}$ can be used to analyze the stability of the system [15]. The poles represent the natural frequencies or modes of the system [16]. The characteristic equation for the system is

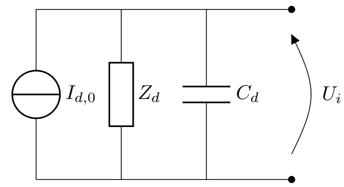

(a) Droop controlled converter

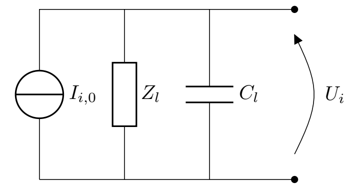

(b) CPL converter

Fig. 4: Linearized Norton equivalent model for droop controlled and constant power load converters.

$$|\boldsymbol{\lambda I} - \boldsymbol{A}| = \boldsymbol{0}. \tag{26}$$

The roots of this characteristic equation depict the poles of the system. A system is stable when it shows an asymptotically decaying behaviour after a perturbation [17]. Hence, the system is stable if all the roots of (26) lie in the left hand side of the $j\omega$-axis.

V. Example Ferry

In this section, an electric ferry is used as a test case for applying the state space modeling method. Two architectures of the distribution system are made of the same ferry – radial and zonal. First, the dynamic model of both the configurations is shown and then stability analysis is done for them.

The main parameters of the ship are given in Table I. There are 6 batteries – each with a capacity of 30.5 kWh. The distribution bus is formed at 662 VDC. In case of bipolar dc grid, the voltage levels are ± 331 VDC. The loads primarily consist of the propulsion motors, bow thruster and auxiliary service loads.

TABLE I: Specifications of the ferry ship.

Equipment	**Specifications**
Source battery	6 x 30.5 kWh
Nominal DC bus voltage	± 331 VDC
Main propulsion motor	2 x 70kW@700 rpm, 100kW@1000 rpm
Bow thruster	24kW @ 2000 rpm

The dc grid of this ship is modelled. The grid in the original ship is unipolar. However, for this paper, a bipolar dc grid is utilized to understand the control and stability of such a grid when two different architectures – radial and zonal – are used.

The length of the ferry is 28 m; the breadth of the ferry is 10 m. The equipment arrangement is such that the batteries lie in the middle of the ferry. The propulsion motors are in the rear side, the bow thruster in at the front. The service loads are distributed across the ferry. However, for this analysis, the dc/ac converter supplying them is located at the front side. The location of the all these loads impact the length of the lines. The information about the line lengths is given in the corresponding sections of the radial and zonal architecture.

A. Radial architecture case

The monopolar version of the dc distribution grid in radial architecture is shown in Fig. 5. The nodes are numbered from n_1 to n_{12}. The lines are numbered from l_1 to l_{11}. The current injected to/from the converters from/to the nodes n_x are denoted by $I_{conv,nx}$.

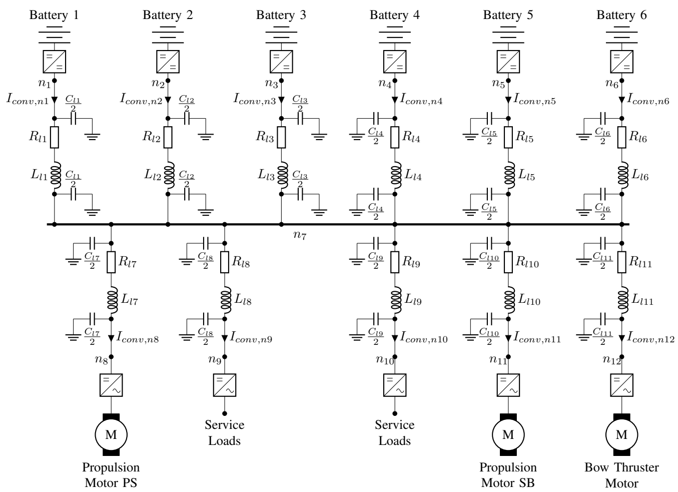

Fig. 5: Model of the ship distribution system in radial architecture showing the line elements.

The cross-section area of all the cables are kept the same at 30 mm^2 to simplify the model. The length of the lines are given in Table II.

TABLE II: Length of lines in radial architecture

Line	Length (m)
l_1 - l_6	5
l_7, l_{10}	15
l_8, l_9	7
l_{11}	10

B. Zonal architecture case

In this section, the test case for the zonal case is developed. The dimension of the ferry and the arrangement of equipment remains the same. However, the cable layout is significantly different in zonal distribution.

Fig. 6 illustrates that the power can be transmitted via two paths in a zonal architecture. There are two feeder paths from the distribution bus. One path goes towards the front of the ferry supplying the service loads and bow thruster drive on the way. The other path goes towards the rear of the ferry supplying the port and starboard side propulsion motor drives.

The model of the grid showing the line elements is shown in Fig. 6. The model constitutes of 22 nodes and 26 lines. The nodes connected to the batteries are the same as in the radial architecture case. However, the nodes for the loads are different.

The cross-section area of the cables is chosen such that the ampacity remains the same as for the radial system. The cross section area of some of the cables is halved as there are two parallel paths to the same loads. On the other hand, the cross section area of some of the lines are increased to match the ampacity. The cross-section area and the length of the lines are given in Table III and IV respectively.

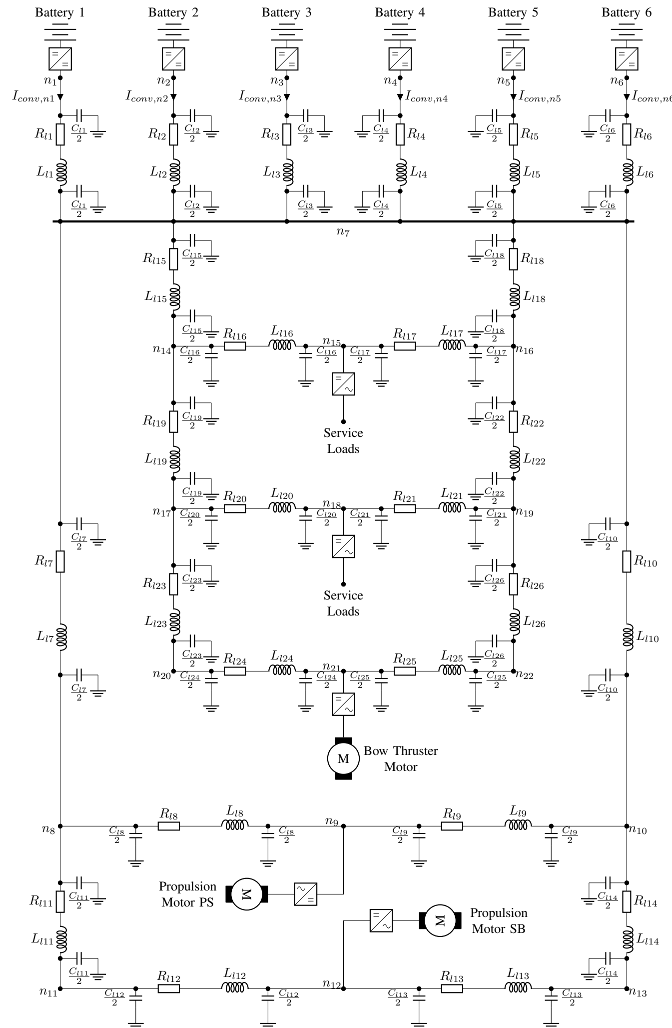

Fig. 6: Model of the ship distribution system in zonal architecture showing the line elements.

TABLE III: Cross-section area of lines in zonal architecture

Lines	Cross-Section Area (mm^2)
l_1 - l_7, l_{10}, l_{19}, l_{22}	30
l_8, l_9, l_{11} - l_{14}, l_{16}, l_{17}, l_{20}, l_{21}, l_{23} - l_{26}	15
l_{15}, l_{18}	45

VI. Test case

A test case was developed for testing the model of the ferry. At 0 ms, there is no current flowing into the system. Also, all the capacitors are charged to ±331 VDC which is the nominal distribution bus voltage of the ferry. At 20 ms, the service loads are turned on. The loads are supplied from

TABLE IV: Length of lines in zonal architecture

Lines	Length (m)
l_1 - l_6, l_8, l_9, l_{12}, l_{13}, l_{15} - l_{18}, l_{20}, l_{21}, l_{23} - l_{26}	5
l_7, l_{10}	10
l_{11}, l_{14}, l_{19}, l_{22}	2

TABLE V: Changes in power in kW at different nodes at different time steps.

Node name	Node Radial	Node Zonal	Time (ms)					
			0	20	40	60	80	100
Battery 2	n_2	n_2	0	0	35	35	0	0
Battery 3	n_3	n_3	0	0	35	35	0	0
Battery 4	n_4	n_4	0	0	0	35	0	0
Battery 5	n_5	n_5	0	0	0	35	0	0
Battery 6	n_6	n_6	0	0	0	35	0	0
Propulsion Motor PS	n_8	n_9	0	0	-70	-70	0	0
Propulsion Motor SB	n_{11}	n_{12}	0	0	0	-70	0	0
Service Loads	n_9	n_{15}	0	-10	-10	-10	-10	0
Service Loads	n_{10}	n_{18}	0	-5	-5	-5	-5	0
Bow Thruster Motor	n_{12}	n_{21}	0	0	0	-25	0	0

the battery pack converters connected to node n_1. At 40 ms, two additional battery pack converters connected to nodes n_2 and n_3 are turned on. Also, the port side propulsion motor drive is turned. At 60 ms, additional battery pack converters connected to nodes n_4, n_5, and n_6 are turned on. Also, the starboard side propulsion motor drive and bow thruster motor drive are turned on. At 80 ms, all the loads except the service loads are turned off. All the battery converters except the droop controlled converter are also turned off. At 100 ms, all the loads are turned off. The power injected/ejected from relevant nodes for radial and zonal configuration are given in Table V.

Each of the converter has three terminals at the output. In these converters the output capacitors are connected between $+$ pole & n pole and n pole and $-$ pole. For simplification, each of the capacitance are set as 400 μF.

VII. Results and Discussion

In this section, the results of the modeling with the test case are illustrated.

A. Simulation

In this section, the dynamic modeling results are shown. The output of the dynamic modeling are shown and discussed. The voltages at relevant nodes and all the line currents for the radial arrangement are shown in Fig. 7 and 8 respectively.

The voltages at relevant nodes and all the line currents for the radial arrangement are shown in Fig. 9 and 10 respectively. The negative currents shown in some of the lines corresponds to the current direction set in the incidence matrix $\boldsymbol{\Gamma}$.

At 0 ms, all the power converters are turned off and no power is being injected/ejected into the system. However, it should be noted that all the capacitors are charged to the system nominal voltage. As only the $+$ pole is shown, the capacitor voltages are $+331$ VDC. At 20 ms, the service loads

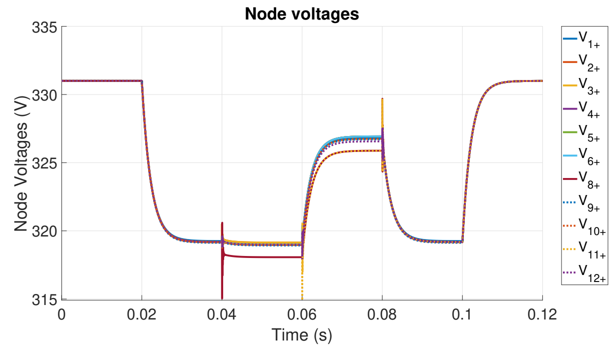

Fig. 7: Voltages at the nodes where source and loads are connected - Radial architecture

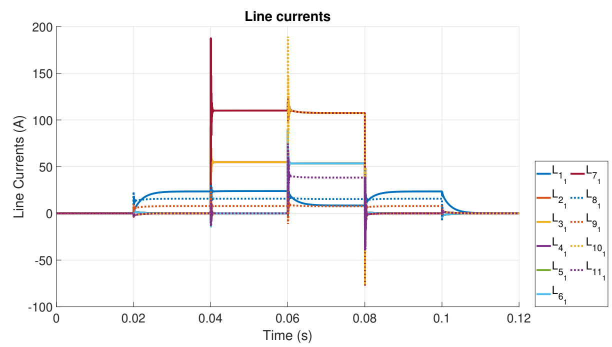

Fig. 8: Currents in all the lines - Radial architecture

connected at nodes n_9 & n_{10} in the radial architecture and at nodes n_{15} & n_{18} in the zonal architecture. Due to this change, the equilibrium voltage of the system changes. This new equilibrium is around $+319$ VDC as shown in Fig 7 and 9. The equilibrium is reached when the derivative of the states become zero. Hence, making the derivatives in (25) zero, we get

$$\begin{bmatrix} \boldsymbol{U_N} \\ \boldsymbol{I_L} \end{bmatrix} = \begin{bmatrix} -\boldsymbol{C}^{-1}\boldsymbol{Z}^{-1} & -\boldsymbol{C}^{-1}\boldsymbol{\Gamma}^{\boldsymbol{T}} \\ \boldsymbol{L}^{-1}\boldsymbol{\Gamma} & -\boldsymbol{L}^{-1}\boldsymbol{R} \end{bmatrix}^{-1} \begin{bmatrix} -\boldsymbol{C}^{-1} \\ \boldsymbol{\emptyset} \end{bmatrix} \boldsymbol{I_{N,0}}. \tag{27}$$

Applying the block matrix principles and decomposing the inverse of state matrix $\boldsymbol{A}$ [14], we get

$$\boldsymbol{U_N} = (\boldsymbol{Z}^{-1} + \boldsymbol{\Gamma}^{\boldsymbol{T}}\boldsymbol{R}^{-1}\boldsymbol{\Gamma})^{-1}\boldsymbol{I_{N,0}}. \tag{28}$$

At 40 ms, the port side propulsion motor is turned on. To balance the power demand by the propulsion motor drive, Battery 2 and Battery 3 are turned on. The equilibrium voltage do not change significantly because the power injected into the system is the same at the power ejected. At 60 ms, all the sources and loads in the systems are turned on. At this time, there is additional 35 kW (compared to the previous state) injected into the system. Hence, the system voltage increases. At 80 ms, all the converters are turned off except the service loads. Hence, the equilibrium states of the system becomes the same as that between 20 ms and 40 ms. At 100 ms, all the converters are turned off and the system returns to its initial state.

The equilibrium voltages are slightly different between the radial and zonal architectures because of the difference between the conductor resistances.

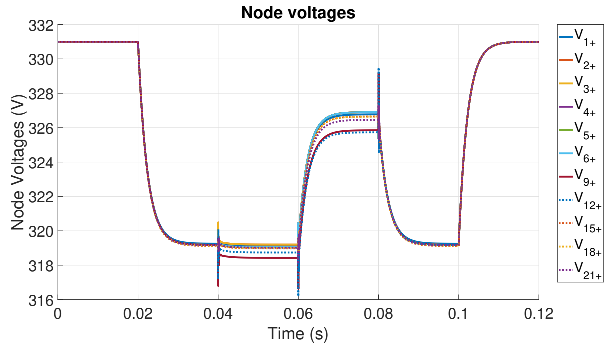

Fig. 9: Voltages at the nodes where source and loads are connected - Zonal architecture

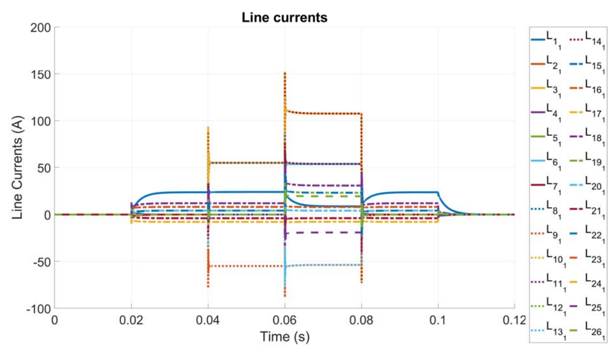

Fig. 10: Currents in all the lines - Zonal architecture

From the first look at the plots for node voltages, we can say that the system is stable in both the architectures. After a change in the node currents ($I_{conv,x}$) – the system state changes. The oscillations in the node voltages and line currents are due to resonance between the system inductance and capacitance. The transient oscillations during a power change are higher in case of the radial architecture compared those in the zonal architecture. This is mainly because the damping of system in zonal architecture is higher. This, in turn, is due to higher resistance of cables because of lower cross-section area as explained in section VI.

B. Stability analysis

As discussed in section IV, the state-matrix $\boldsymbol{A}$ can be used to find the poles of the system. For the radial and zonal architectures, the poles of the system are illustrated in Fig. 11 and Fig. 12 respectively.

Several differences are present between the pole plots of both the systems. There are more poles of the zonal architecture. This is because of the higher number of nodes and lines in this system. The poles farther away from the $j\omega$-axis appear

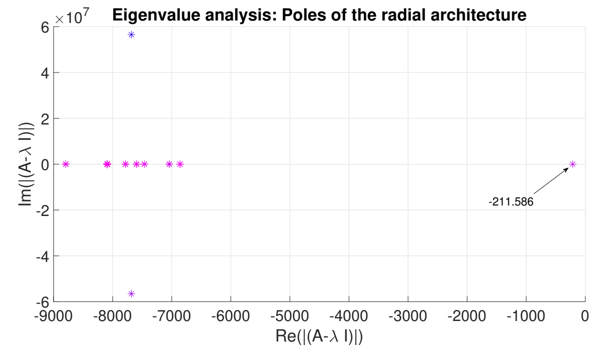

Fig. 11: Poles of the system for radial architecture of ferry.

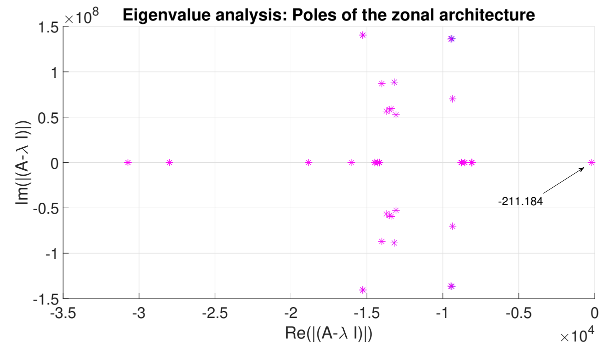

Fig. 12: Poles of the system for zonal architecture of ferry.

due to the line elements (inductances and capacitances) and converter capacitances. These poles represent the frequencies of oscillations appearing in the line currents and voltages when the system state changes. The amplitude of oscillation becomes smaller and smaller when the poles move more and more towards the left of $j\omega$-axis [18]. In the zonal architecture, most of the poles are farther away from the $j\omega$-axis compared to the radial architecture. This implies that the oscillations are dampened more in the zonal architecture compared to the radial architecture as is discussed in section VII-A.

In Fig. 11 and 12, there is a pole which is present close to the $j\omega$-axis. This pole appear due to the droop controlled converter in the system. The position of this pole is similar in both the architectures because the droop impedance of the converter is the same. This is a slow pole and significantly impacts the stability of the system. The pole has a tendency to move closer to the $j\omega$-axis if the value of droop impedance is increased. Consequently, the droop impedance should be high enough for a stable dc grid.

VIII. Conclusion

In this paper, a dynamic modeling technique is utilized to model dc grids on ships. State-space method is used for this purpose. Due to space considerations, only the plots for the positive pole are shown. The stability analysis of a dc grid using the state matrix is also discussed. The modeling method is used to simulate two power distribution architectures on a ferry – radial and zonal. The results of the simulation show that there are lower voltage oscillations in zonal architecture compared to the radial architecture. The stability analysis of the two architectures also show that the poles of the zonal architecture system are faster than those of the radial architecture system. Hence, it can be said that the zonal architecture with the same number of components and line length is more stable compared to the radial architecture.

There are however, limitations to the analysis. Firstly, the impedance characteristics of the converters are taken for the linearized cases which are not frequency dependent. Also, the dynamics of the power converters are neglected. An improved model would contain the dynamics of the converters as well.

In this study, it is concluded that zonal dc architectures can provide better performance than radial dc architectures. A zonal architecture is a meshed dc grid and has several advantages compared to a radial grid such as reduced possibility of congestion in the network [19]. However, there are several challenges regarding the implementation of zonal architectures with respect to the power flow control and protection of the system [20]. Hence, the realization of zonal dc grids can take some time for general acceptance in the industry.

REFERENCES

[1] T. Smith, J. Jalkanen, B. Anderson, J. Corbett, J. Faber, S. Hanayama, E. O'keeffe, S. Parker, L. Johanasson, L. Aldous *et al.*, "Third IMO GHG Study," 2014.

[2] S. Lin, "Greenhouse gas mitigation strategies - a ship operator's perspective in the container shipping industry." p. 72, 2012.

[3] DNV-GL, "Maritime forecast to 2050," *Energy transition outlook*, vol. 2018, 2018.

[4] E. A. Bouman, E. Lindstad, A. I. Rialland, and A. H. Strømman, "State-of-the-art technologies, measures, and potential for reducing GHG emissions from shipping – A review," *Transportation Research Part D: Transport and Environment*, vol. 52, pp. 408–421, May 2017. [Online]. Available: https://linkinghub.elsevier.com/retrieve/pii/S1361920916307015

[5] H. Pestana, "Future trends of electrical propulsion and implications to ship design," in *Maritime Technology and Engineering*, C. Soares and T. Santos, Eds. CRC Press, Sep. 2014, pp. 797–803. [Online]. Available: http://www.crcnetbase.com/doi/abs/10.1201/b17494-105

[6] G. Chang, Y. Wu, S. Shao, Z. Huang, and T. Long, "DC Bus Systems for Electrical Ships: Recent Advances and Analysis of a Real Case," *IEEE Electrification Magazine*, vol. 8, no. 3, pp. 28–39, Sep. 2020. [Online]. Available: https://ieeexplore.ieee.org/document/9185056/

[7] K. Kim, K. Park, G. Roh, and K. Chun, "DC-grid system for ships: a study of benefits and technical considerations," *Journal of International Maritime Safety, Environmental Affairs, and Shipping*, vol. 2, no. 1, pp. 1–12, Nov. 2018, cites: kimDCgridSystemShips2018. [Online]. Available: https://www.tandfonline.com/doi/full/10.1080/25725084.2018.1490239

[8] G. van den Broeck, "Voltage control of bipolar DC distribution systems," Ph.D. dissertation.

[9] E. W. Kimbark, *Direct current transmission*. Wiley, 1971, vol. 1.

[10] N. H. van der Blij, L. M. Ramirez-Elizondo, M. T. Spaan, and P. Bauer, "A state-space approach to modelling dc distribution systems," *IEEE Transactions on Power Systems*, vol. 33, no. 1, pp. 943–950, 2017.

[11] M. Zubiaga, G. Abad, J. Andoni, S. Aurtenetxea, and A. Crcar, "Evaluation of the Frequency Response of AC Transmission Based Offshore Wind Farms," in *Wind Farm - Impact in Power System and Alternatives to Improve the Integration*, G. O. Suvire, Ed. InTech, Jul. 2011.

[12] B. Friedland, *Control system design: an introduction to state-space methods*, dover ed ed. Mineola, NY: Dover Publications, 2005.

[13] A. Emadi, A. Khaligh, C. Rivetta, and G. Williamson, "Constant Power Loads and Negative Impedance Instability in Automotive Systems: Definition, Modeling, Stability, and Control of Power Electronic Converters and Motor Drives," *IEEE Transactions on Vehicular Technology*, vol. 55, no. 4, pp. 1112–1125, Jul. 2006.

[14] N. van der Blij, L. Ramirez-Elizondo, M. Spaan, and P. Bauer, "Stability of DC Distribution Systems: An Algebraic Derivation," *Energies*, vol. 10, no. 9, p. 1412, Sep. 2017.

[15] P. Kundur, "Power system stability," *Power system stability and control*, pp. 7–1, 2007.

[16] G. F. Franklin, J. D. Powell, A. Emami-Naeini, and J. D. Powell, *Feedback control of dynamic systems*. Prentice hall Upper Saddle River, NJ, 2002, vol. 4.

[17] T. Dragičević, X. Lu, J. C. Vasquez, and J. M. Guerrero, "DC Microgrids–Part I: A Review of Control Strategies and Stabilization Techniques," *IEEE Transactions on Power Electronics*, p. 17, 2015.

[18] L. O. Chua, C. A. Desoer, and E. S. Kuh, *Linear and Nonlinear Circuits*, ser. McGraw-Hill Series in Electrical Engineering. New York: McGraw-Hill, 1987.

[19] L. Mackay, N. H. v. d. Blij, L. Ramirez-Elizondo, and P. Bauer, "Toward the universal dc distribution system," *Electric Power Components and Systems*, vol. 45, no. 10, pp. 1032–1042, 2017.

[20] L. Mackay, T. Hailu, L. Ramirez-Elizondo, and P. Bauer, "Decentralized current limiting in meshed dc distribution grids," in *2015 IEEE First International Conference on DC Microgrids (ICDCM)*. IEEE, 2015, pp. 234–238.